PNAS RESEARCH ARTICLE | CHEMISTRY ENVIRONMENTAL SCIENCES OPEN ACCESS

Ultrabroadband plasmon driving selective photoreforming of methanol under ambient conditions

Nasir Uddin[a,1], Zhehao Sun[a,b,1], Julien Langley[a], Haijao Lu[a], Pengfei Cao[c,2], Ary Wibowo[d], Xinmao Yin[e,f], Chi Sin Tang[g], Hieu T. Nguyen[d], Jack D. Evans[h], Xinzhe Li[i], Xiaoliang Zhang[j], Marc Heggen[c], Rafal E. Dunin-Borkowski[c], Andrew T. S. Wee[f], Haitao Zhao[b,2], Nicholas Cox[a], and Zongyou Yin[a,2]

Edited by Alexis Bell, University of California, Berkeley, CA; received July 14, 2022; accepted November 1, 2022

Liquid methanol has the potential to be the hydrogen energy carrier and storage medium for the future green economy. However, there are still many challenges before zero-emission, affordable molecular H_2 can be extracted from methanol with high performance. Here, we present noble-metal-free Cu–WC/W plasmonic nanohybrids which exhibit unsurpassed solar H_2 extraction efficiency from pure methanol of 2,176.7 μmol g^{-1} h^{-1} at room temperature and normal pressure. Macro-to-micro experiments and simulations unveil that local reaction microenvironments are generated by the coperturbation of WC/W's lattice strain and infrared-plasmonic electric field. It enables spontaneous but selective zero-emission reaction pathways. Such microenvironments are found to be highly cooperative with solar-broadband-plasmon-excited charge carriers flowing from Cu to WC surfaces for efficient stable CH_3OH plasmonic reforming with C_3-dominated liquid products and 100% selective gaseous H_2. Such high efficiency, without any CO_x emission, can be sustained for over a thousand-hour operation without obvious degradation.

plasmonic methanol reforming | broad solar spectrum | strain-electric field | hydrogen | microenvironments

Significance

Photoreforming of methanol has been envisioned as a promising pathway to produce H_2 fuel which gained interest over the years. However, the formation of CO_2/CO byproducts from this pathway has seen as a major hurdle to its practical realization because the evolution of CO_2 and/or CO gases will negatively contribute toward the global-warming and/or environmental issues. To resolve these issues, herein, we discovered solar-driven ultrabroadband plasmonic photoreforming of pure methanol to pure, green and self-separable H_2 energy production with zero-emission from an all-plasmonic Cu–WC/W catalytic system. The local electric field, lattice misfit strain, and the monodirectional flow of charge carriers by optical dielectric gradient work in synergy to enable the superior plasmonic photocatalysis in this all-plasmonic system.

Photocatalytic (PC) wireless/direct solar to H_2 fuel production has been championed as a promising modern clean energy technology (1, 2). To take PC pure water splitting to H_2 fuel as an example, the study started in 1986, which reported the first kind of photocatalysts with TiO_2 on the positive polar ferroelectric substrate (3). Since then, enormous research efforts have been devoted to this area, with the typical works summarized in *SI Appendix*, Table S1. Admittedly, progress has been made in the past thirty-five years. However, barriers to the practical applications of this technology remain mainly due to the limited solar-to-hydrogen (STH) efficiency, poor durability of photocatalysts, and/or the affordability issue (1, 2, 4). This is associated with, e.g., sluggish four-electron-involved redox kinetics and dynamics, poor photochemical stability in aqueous environments, and reliance on expensive noble metals which hinder scalability (5, 6). Beyond water splitting, relatively less well-studied alternative processes for PC H_2 fuel production show promise, for instance, dehydrogenation of ammonia (7), methanol (8–10), ethanol (11), and formic acid. Many of these substitute methods are also viewed as tools for simultaneously managing carbon emission and H_2 production. However, further work remains to be done to optimize these processes for commercial applications.

Among these processes, the PC production of H_2 from pure methanol shows particular promise in terms of practical implications. It has several unique advantages: 1) no strong C–C bonds facilitating dehydrogenation under mild conditions; 2) rich gravimetric hydrogen content (12.6%); 3) it is liquid under ambient conditions and thus compatible with existing infrastructures for storage and transportation; 4) the thermodynamic ease of its two-electron redox reaction (9); and 5) lack of obvious hydrolysis or corrosion of catalysts in photoredox reactions with methanol. To date, PC generation of H_2 from pure methanol has been reported at high temperatures (so-called photothermal reaction) (12) and room temperature (8, 13). However, issues of CO_x emission, cost-competitivity (noble metals, or UV reliance), and catalyst lifetime have thus far limited its utility. Recently, our work on noble-metal-free materials has highlighted the possibility of improving catalytic lifetime and efficiency by employing visible-light-responsive single-layer semiconductors of MoS_2 (14) and C_3N_4/SnS heterojunction with Z-scheme band profiles (15). Admittedly, the currently achieved performance of these materials is still far behind the demands of industrialization, leaving a research gap in this area.

Advancements in nanomaterial synthesis now allow catalysts with complex architectures and materials with integrated multifunctionality to be manufactured (16), which provides rich space for reaction microenvironment engineering. The microenvironment engineering

Competing interest statement: The authors declare a competing interest. The authors have patent filings to disclose. The authors declare that an Australian provisional patent application 2022903604 has been filed on 28 November 2022 for the technique related to this work.

This article is a PNAS Direct Submission.

[1]N.U. and Z.S. contributed equally to this work.

[2]To whom correspondence may be addressed. Email: p.cao@fz-juelich.de, ht.zhao@siat.ac.cn, or zongyou.yin@anu.edu.au.

This article contains supporting information online at https://www.pnas.org/lookup/suppl/doi:10.1073/pnas.2212075120/-/DCSupplemental.

Published January 12, 2023.

has been used with great success in electrocatalysis (17) and can be extended to photocatalysis, which additionally involves light–matter interaction with the potential to generate local electric field (E-field), for example, from plasmonic materials. Simultaneous tailoring of both photochemical properties and reaction microenvironments will open up next-generation multifunctional photocatalysts, including plasmonic ones, with enhancing performance for solar H_2 fuel generation from pure methanol.

In this work, we designed and fabricated a multicomponent plasmonic nanohybrid consisting of Cu nanoparticles (NPs) and WC/W NPs which efficiently catalyzes the generation of H_2 from pure methanol. We hypothesize that this enhanced performance can be attributed to the synergy of the introduced reaction microenvironments and plasmonic photocatalysis. These include the following: 1) The formation of a strain effect from core W to shell WC structure in the WC/W core–shell composite. 2) Plasmonic WC/W leads to a localized surface plasmon resonance (LSPR) which induces E-field around the WC surface. 3) Improved solar spectrum utilization owing to the absorption characteristics of plasmonic Cu NPs. This should lead to more charged carriers effectively flowing from Cu NPs to shell WC due to their different dielectric properties, thus enabling redox reactions during methanol photoreforming. The combination of the strain and E-field microenvironments selectively lowers the kinetics barriers compared to side pathway reactions, avoiding CO_x formation. Such cooperative effects result in superior PC reactivity and selectivity. Parallel computational work supports these findings and further elaborates on how the microenvironments perturb the reaction pathways and how the plasmonic structure arrangements dictate the photoexcited charge carrier contributions to the CH_3OH photoreforming reactions.

Results

Catalysts Preparation and Characterization. We begin by preparing plasmonic Cu–WC/W nanostructure using a carburization process at high temperature under a vacuum-hydrogen atmosphere (*SI Appendix*, Supporting text). Experimental parameter optimization reveals that the 2% Cu–WC/W nanohybrid loading performs best (*SI Appendix*, Figs. S1–S3). X-ray diffraction (XRD) patterns verify the successful formation of Cu–WC/W nanohybrid structures (*SI Appendix*, Fig. S4).

Using the aberration-corrected high-resolution TEM technique, we have analyzed microstructural properties of representative in situ prepared WC/W NPs (*SI Appendix*, Fig. S5). The WC/W NPs have an average particle size of ~56 nm (*SI Appendix*, Figs. S5 *A* and *B* and S6). Representative W components show that W is primarily formed in the [111] direction (*SI Appendix*, Fig. S5 *C* and *D*), whereas WC is identified in [110] direction (*SI Appendix*, Fig. S5 *E* and *F*). We also noticed that WC NPs might have some lattice distortion, which could be associated with the presence of W atoms inducing strain by the atomic lattice mismatch as shown in *SI Appendix*, Fig. S5*E* and Fourier transform analysis (*SI Appendix*, Fig. S5*F*). Because the WC layer is thin and at the surface of W, lattice distortions occur. Note that the formed WC nanostructure is dominated by small crystal domains with slight amorphous, which is well aligned with XRD results. The microstructural results show that the metallic W formed a core while WC formed a shell. *SI Appendix*, Fig. S5*G* shows a TEM image of an optimized 2% Cu–WC/W sample which highlights randomly scattered particles, having an average size of ~45 nm (*SI Appendix*, Fig. S7). Cu NPs are observed on the surface of the WC layer as shown in *SI Appendix*, Fig. S5*H*, corresponding to an average size of 4 to 6 nm (*SI Appendix*, Fig. S8), which is comparable to the size of pure Cu NPs (*SI Appendix*, Fig. S9). The phase components WC, W, and Cu are analyzed in more detail in the enlarged high-resolution TEM image of *SI Appendix*, Fig. S5*I*. The Cu NPs show a lattice spacing of 0.21 nm, and its zone axis is indexed along the [011] direction (*SI Appendix*, Fig. S5*I* and inset FFT image). A closer inspection of *SI Appendix*, Fig. S5 *H* and *I* reveals that Cu NPs are primarily formed at the shell and not at the W core. This might be attributed to the immiscibility of Cu with elemental W (18).

A high-angle annular dark-field transmission electron microscopy (HAADF-STEM) image of the 2% Cu–WC/W sample reveals a local epitaxial growth of the WC shell on the W core (Fig. 1*A*). It is suggested that the carbide formation in the presence of carbon under reducing agents like H_2 gas can mediate in situ heteroepitaxial growth at high temperatures (19). The epitaxial growth of WC and W in the gas-phase deposition could originate from the lattice mismatch, resulting in the formation of a hybrid core–shell nanostructure. Depending on the degree of lattice misfit, the resulting interface between two materials can be coherent to noncoherent (20). Fig. 1*B* reveals the epitaxial growth boundary between WC and W whereas a semicoherent growth of WC on the {011} plane of pure W. The misfit along the plane {110} is 12% for the WC layer. Similarly, during the epitaxial growth along with W {101} plane (Fig. 1*C*), the lattice distance of WC in the {001} plane expanded 0.28 nm, and the lattice misfit in the latter case is about 21%. In contrast to the present study, a core Au and shell CdS nanostructure with up to 43% lattice misfit was reported previously (21). Furthermore, the resolved TEM image (Fig. 1*D*) and FFT analysis of WC particles (Fig. 1*E*) contain a single diffraction peak in [110] direction of WC, which highlights the compressive strain from W. Moreover, the representative W in the composite exhibits similar diffraction data (Fig. 1 *F* and *G*) as observed for WC, confirming a semicoherently strained epitaxial overgrowth resulting in the formation of a core–shell nanohybrids structure. Such lattice strain at nano regime could behave as the reaction microenvironment which is believed to mediate PC activities for pure methanol reforming. In addition, STEM-EDX elemental mapping shows the coexistence of W, C, and Cu in the composite (Fig. 1*H*), whereas the bare WC/W sample exhibits the presence of W and C (*SI Appendix*, Fig. S10).

Physicochemical Properties Analysis. X-ray photoelectron spectroscopy (XPS), X-ray absorption near edge structure (XANES), and extended X-ray absorption fine structure spectroscopy (EXAFS) were performed to verify the local chemical composition of the catalysts. *SI Appendix*, Fig. S11 *A* and *B* shows fine W 4f spectrums with and without Cu addition, which can be fitted into multiple peaks in the range of 30 to 40 eV, indicating the mixed chemical oxidation states of the W atom. The peaks located at binding energies of 31.46 (W $4f_{7/2}$) and 33.67 eV (W $4f_{5/2}$) are assigned to the metallic W while the peaks at 31.88 and 34.10 eV correspond to W–C bond (WC) (22), and those at higher binding energies of 36.04 (W $4f_{7/2}$) and 38.07 eV (W $4f_{5/2}$) are attributed to unavoidable surface oxidation of tungsten carbide when the samples were exposed to air during their storage, transportation, and XPS operation (23). Furthermore, the C 1s spectrum of catalysts before and after Cu introduction revealed similar atomic composition in the nanohybrids (*SI Appendix*, Fig. S12). The XPS profile of the Cu 2p region (*SI Appendix*, Fig. S11*C*) exhibits two prominent peaks at 932.57 and 952.37 eV in a 2:1 area ratio, representing the electron-splitting energies of Cu $2p_{3/2}$ and Cu $2p_{1/2}$, respectively, which is a typical feature of the Cu^0 state (24). The absence of shake-up satellites between 940 and 945 eV (24) and other

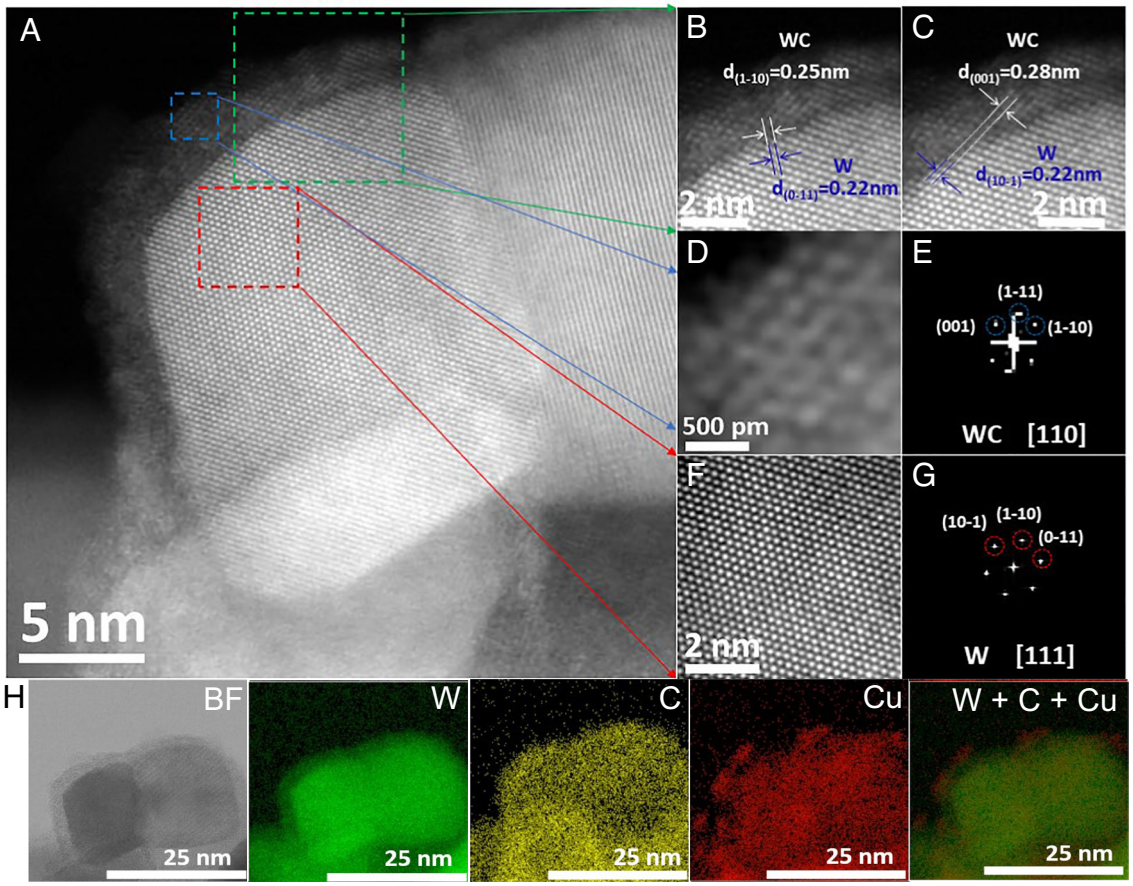

Fig. 1. Microstructural characterization. (*A*) HAADF-STEM images of a Cu–WC/W sample. (*B*) and (*C*) Cropped area near the epitaxial boundary of W and WC components, and the epitaxial relationship between W and WC. (*D*) Representative WC particles. (*E*) The corresponding FFT pattern of W. (*F*) representative W component. (*G*) The corresponding FFT pattern of W. (*H*) Bright-field (BF) image of 2% Cu–WC/W sample and EDX elemental maps of W, C, Cu, and W+C+Cu.

characteristic peaks ascribed with Cu^{2+} for Cu $2p_{3/2}$ and Cu $2p_{1/2}$ were not identified at around 942.2 and 962.0 eV (25), indicating that there are no Cu^{2+} species formed. To verify the Cu state for the prepared photocatalysts, the X-ray-excited Auger electron spectroscopy was performed and found that the dominated peak of Cu $L_3M_{4,5}M_{4,5}$ spectra is located at 918.50 eV which is indicative that the state of Cu species is metallic (*SI Appendix*, Fig. S11*D*) (26). XANES analysis shows that an intense peak at 8,992.95 eV corresponds to a so-called white-line peak, signaling a greater number of coordination numbers in the first shell of the cation and a more uniform bond length distribution Fig. 2*A* (27). The Fourier transform (FT) of the Cu–K edge with fitted data (Fig. 2 *B* and *C*) shows an intense peak at R< 2.81 Å, but the absence of well-defined features at R > 2.81 Å supports the assignment of large structural disorder beyond the first shell surrounding the central atom (28). This effective radial distribution strongly suggests that under H_2 annealing conditions at 850 °C, the copper species are fully reduced to metallic Cu^o without any Cu–O formation (29). By further performing quantitative EXAFS analyses, we estimate an average Cu–Cu bond length of 2.41 Å with a coordination number of 12 which is in good agreement with the fcc structure of Cu elements (30).

Fig. 2*D* shows the real (ε_r) and imaginary (ε_i) parts of the dielectric properties of Cu and WC samples, respectively. Comparison of complex refractive index and extinction coefficient of Cu, WC, and W samples reveal that due to low n and k values, the Cu NP sample shows improved light harvesting features (*SI Appendix*, Figs. S13–S16 and *Supporting text*). The Cu NPs show smaller ε_i values as compared with WC and W (Fig. 2*D* and *SI Appendix*, Fig. S16) in the entire visible spectrum, indicating that energetic charge carriers from Cu's LSPR could flow from Cu to the neighboring WC by dissipating the energy via plasmon decay (31). Theory suggests that under plasmonic excitation, the photoinduced charge carriers dissipate their stored energy to the reactant molecules and perform multifaceted photoactivities which depend on the charge carrier's dynamics (31). Fig. 2*E* reveals that the characteristic semicircular spectrum of the 2% Cu–WC/W sample is significantly compressed, demonstrating improved charge carrier kinetics at the plasmonic NPs interface. Additionally, ultraviolet photoelectron spectroscopy measurement exhibits work function values of 4.57 and 4.34 eV for WC/W and 2% Cu–WC/W samples, respectively, relative to vacuum (Fig. 2*F*). This highlights the established energy equilibrium between Cu NPs and the metallic WC/W junction, resulting in the built-in step potential for charge carrier migration across the plasmonic nanohybrids interface.

Optical and Plasmonic Properties Measurement of Photocatalysts. Development of plasmonic Cu-based NPs along with metallic WC/W nanostructures, as demonstrated above, is a significant step toward utilizing the full solar spectrum due to their broadband LSPR spanning from UV to visible and to near-infrared (NIR) regions. Fig. 3*A* shows the absorption peak of WC/W primarily located 400 to 550 nm, indicating that it can accumulate light energy mainly in the visible range. This is in sharp contrast with previous results which showed very flat or negligible absorption spectra for metallic carbides (32). However, the metallic Cu NPs show a very broad spectrum covering from 400 to 1,000 nm,

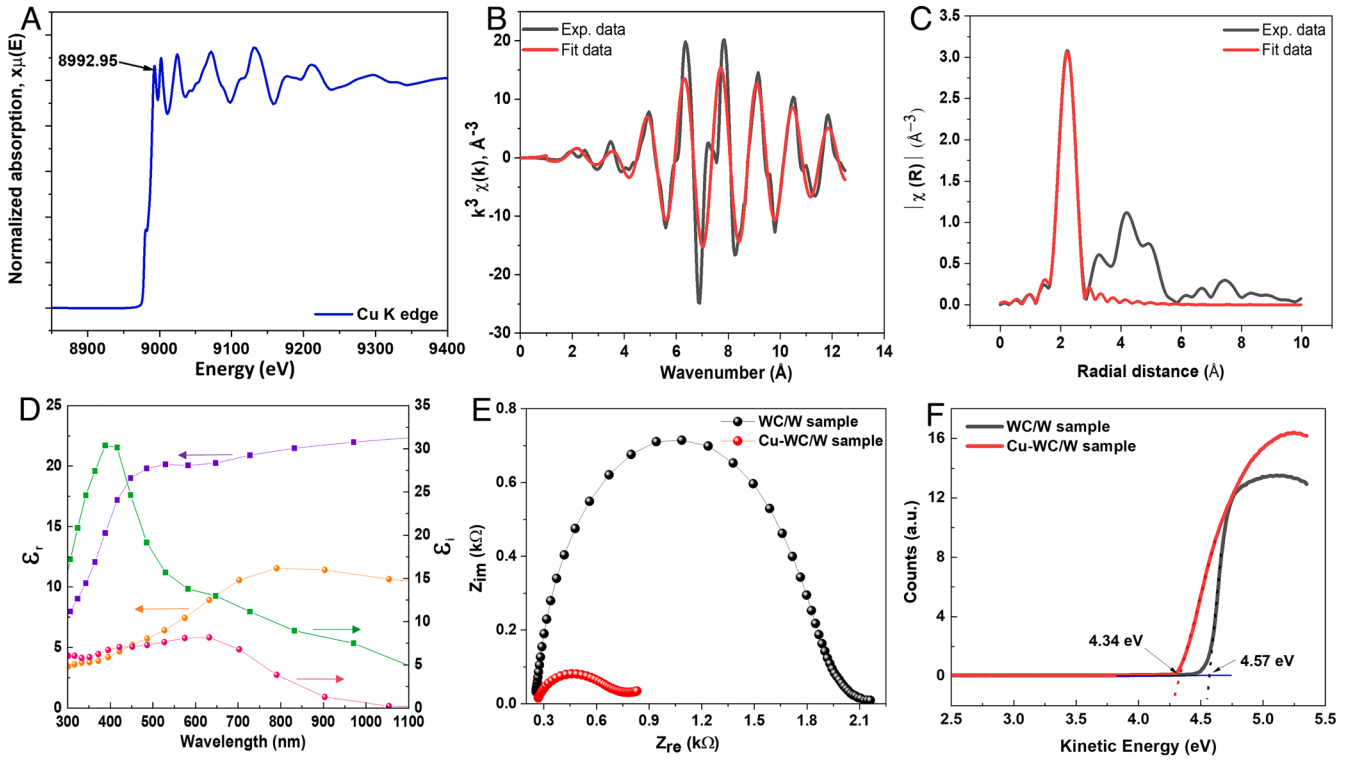

Fig. 2. Physicochemical properties measurement of the plasmonic photocatalysts. (*A*) Normalized Cu K-edge XANES spectra. (*B*) k^3-weighted FT EXAFS spectra obtained in the range of 3 to 10.55 $Å^{-1}$. (*C*) Magnitude of the Fourier transform (FT) of k^3 χ(k) in the R space. Fitting was done only for first shell. The parameters were used for EXAFS fitting as follows: E_o = 4.12096998 ± 0.57813727; ΔR = −0.01496875 ± 0.00376265; S_0^2 = 0.85100400 ± 0.05035596; R-factor = 0.0008586; σ^2 = 0.00871232 ± 0.0053552; reduced chi-square = 94.995387; number of variables = 4. (*D*) dielectric properties of Cu (filled circle) and WC (filled square box) sample. (*E*) Nyquist plot of WC/W and 2% Cu–WC/W. (*F*) Ultraviolet photoelectron spectroscopy profile for WC/W and 2% Cu–WC/W samples.

indicating a significant light absorption ability. The strong light absorption capacity of the composite is the indication of LSPR features, which rely on NPs sizes. It was highlighted that as NPs sizes get smaller, the Cu NPs show broad solar light absorption resulting in strong LSPR effects, whereas the resonance absorption efficiency gets weaker as NP sizes increase because of scattering effects (33, 34). Examples of broad solar light absorption features of Cu NPs can be found elsewhere (34, 35). In these examples, C was present as a shell that protects the Cu NPs from being oxidized and widens the light absorption performance of the core–shell nanostructure (34, 36, 37). These results directly indicate that the utilization of ultrabroadband solar flux ranging from UV to NIR photons over 2% Cu–WC/W is feasible.

To study the behaviors of LSPR, the plasmonic Cu–WC/W NPs were investigated by STEM-monochromated EELS (Fig. 3 *B* and *C*). EELS spectra were measured near the surfaces of target particle regions, where sites A and B are located near the WC shell, while site C is near an individual Cu NP on the WC/W surface (Fig. 3*B*). As shown in Fig. 3*C*, the WC/W NP exhibits a strong peak in region 1 [~ 0.6 to 0.9 eV, short-wave IR (SWIR)], weak and broad peaks in region 2 (~1.0 to 1.5 eV, NIR) and region 3 (~1.9 to 2.7 eV, VIS). Interestingly, since WC has a strong light absorption with wavelengths greater than 1,000 nm (38), an unexpectedly strong peak at SWIR in region 1 implies that relatively low-energy plasmonic resonance exists in the WC/W structure, which is beyond the measurement scope of our UV-DRS. In addition, tungsten was also found to be a NIR absorber (39), so the prepared WC/W nanostructure is supposed to be responsive to NIR light, as observed by the peak at region 2. The EELS spectrum in region 3 is a broad weak peak associated with the visible-light absorption, which is also observed in the UV-DRS absorption spectrum from WC/W in Fig. 3*A*. Sites A and B exhibit similar EELS spectra, indicating the good uniformity of WC shell on W core nanostructure. To evaluate the LSPR-induced surface E-field intensity for the three regions, we performed finite-difference time-domain (FDTD) simulation for these three different energy ranges and the corresponding peak positions of the incident light. From the results in Fig. 3 *D*–*F*, there does not exist an obvious difference in E-field distribution between them, implying that LSPR from WC/W is not wavelength sensitive. Therefore, the much higher intensity of LSPR from the SWIR (region 1) is supposed to dominate the contribution to E-field for WC/W. Furthermore, when the electron beam was placed near to Cu NP, the EELS spectra in both regions 2 and 3 were obviously enhanced, consistent with the absorption feature variation from WC/W to Cu–WC/W as shown in Fig. 3*A*, which indicates that the absorption of visible to NIR region from Cu NPs contributed to the overall light absorption of the whole plasmonic Cu–WC/W system. This shows that the two components of Cu and WC/W work in synergy in the absorption of light covering different wavelengths with generating their LSPRs which will tailor pure methanol photoreforming reaction at the nanoscale.

Sustained PC Activity. As depicted in Fig. 4*A*, we measured the H_2 production yield for six consecutive cycles where each cycle lasted for about 168 h and involved illumination under white light passed through an AM 1.5 G filter. The H_2 production escalated over the illuminated period up to 120 h where it plateaued. This could be explained by the fact that the in situ-formed H_2 in the volume-constant sealed reactor will increase the gaseous partial pressure, resulting in sluggish methanol activities (14, 15). Quantitatively, however, within the first 2 h of irradiance of

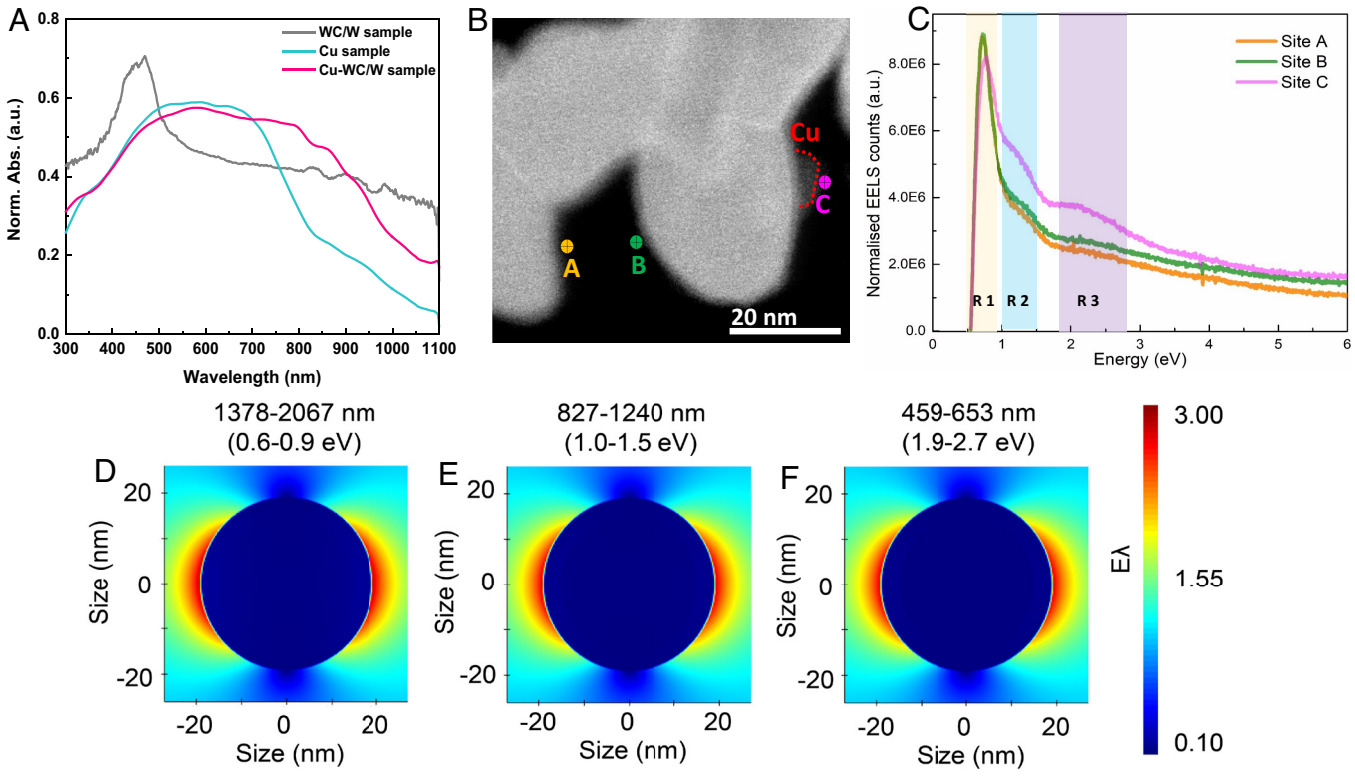

Fig. 3. Optical and plasmonic properties measurement of photocatalysts. (*A*) Normalized absorption spectrum of WC/W, Cu, and 2% Cu–WC/W photocatalysts. (*B*) ADF image of Cu–WC/W sample, sites A, B and C are the locations where EELS spectrum obtained near WC shell and Cu NP, respectively, and Cu particle is indicated by the red curved dashed line. (*C*) Low loss EELS spectra obtained from sites A, B, and C indicated in the ADF image. R1, R2, and R3 represent peak regions 1, 2, and 3, respectively. (*D*)–(*F*) The FDTD E-field distribution simulation results for WC/W system with light illumination under different wavelength ranges: (*D*) region 1 [~1,378 to 2,067 nm corresponding to ~0.6 to 0.9 eV, short-wave IR (SWIR)], (*E*) weak and broad peaks in region 2 (~827 to 1,240 nm corresponding to ~ 1.0 to 1.5 eV, NIR), and (*F*) region 3 (~459 to 653 nm corresponding to ~ 1.9 to 2.7 eV, VIS), where the E-field intensity of incident light was set as 1 V/m.

solar light, the produced H_2 was 8.7 μmole, extending to 22.4 μmole after 120 h of reaction. In terms of PC efficiency, this can be expressed from 2176.7 to 93.4 μmole.g^{-1}.h^{-1} over identical illuminated time (*SI Appendix*, Fig. S17). Impressively, all six cycles maintained their undifferentiated recyclability, still ensuring ~96 % of the initially observed activity. This equates to more than 1,000 h of endurable activity (*SI Appendix*, Fig. S18), which has been rarely reported for this reaction to date (*SI Appendix*, Table S1). Compared to WC/W and bare Cu, the photoactivity increased by almost 14 and 47 fold, respectively (*SI Appendix*, Fig. S2). Estimated solar to hydrogen conversion efficiency was 2.37%, indicating a sizeable volume of incident photon energy (11.20%) was utilized (*SI Appendix*, Supporting text). This result is outstanding. The unsurpassed PC performance is attributed to the highly stable nanoheterointerface between plasmonic Cu NPs and the WC/W NPs junction, which altogether shows an uncommon promotional impact on the surface active sites of the catalysts. To verify this stability, we have performed a hot filtration test which shows that the as-prepared plasmonic Cu–WC/W nanohybrid structure is highly heterogeneous in nature and there is no leaching of the particles from the original nanostructures (*SI Appendix*, Fig. S19). Moreover, the longevity of 2% Cu–WC/W photocatalysts was also confirmed from ICP, XPS, SEM, and TEM tests based on the sample after PC reaction, which shows that after 168 h of methanol photoreforming, the structures of PC materials were well remained (*SI Appendix*, Figs. S20–S22 and *Supporting text*). Notably, the broad light absorption feature of the 2% Cu–WC/W NPs is considered to be a determining factor for catalysis improvement, which proliferated/excited charge carriers with different (low to high) kinetic energy for redox reactions (40). To rule out whether the thermal effect contributes to the catalytic performance, the external heating experiment was performed at different temperatures. The evaluation of the thermal experiments revealed that the thermal/temperature effect has negligible influence on methanol decomposition to hydrogen at the catalyst surface (*SI Appendix*, Fig. S23). This validates that the photodehydrogenation of methanol in this system is primarily induced by the photoexcited charge carriers at the NP surface.

Following this excellent stability of 2% Cu–WC/C NPs, we have performed chopped photocurrent measurements at various illuminated conditions as shown in Fig. 4 *B* and *C*. Differences in photocurrent activities were observed at different illumination conditions. For example, the photocurrent at AM 1.5 G was increased by 36.42, 69.41, and 77.32%, as compared at 420, 700, and 800 nm, respectively. These results directly prove that the broadband plasmon-driven visible-light photoresponsivity was larger with a broader light absorption of 2% Cu–WC/W NPs at AM 1.5 G conditions. On the other hand, the photocurrent differences at 420, 700, and 800 nm could be related to the different light power intensity the sample received from the band pass filters (*SI Appendix*, Fig. S3). Notably, under AM 1.5 G simulated sunlight conditions, the photocurrent from 2% Cu–WC/C NPs was enhanced by 96.56% as compared with bare WC/W sample (*SI Appendix*, Fig. S24).

We observed methylal ($C_3H_8O_2$) and methyl formate ($C_2H_4O_2$) as liquid products alongside self-separable H_2 gas (Fig. 4*D* and *SI Appendix*, Fig. S25). Selectivity is a descriptor to explain the preferential product formation in the system. So, the selectivity of these products was estimated to be 80.94% for $C_3H_8O_2$ whereas

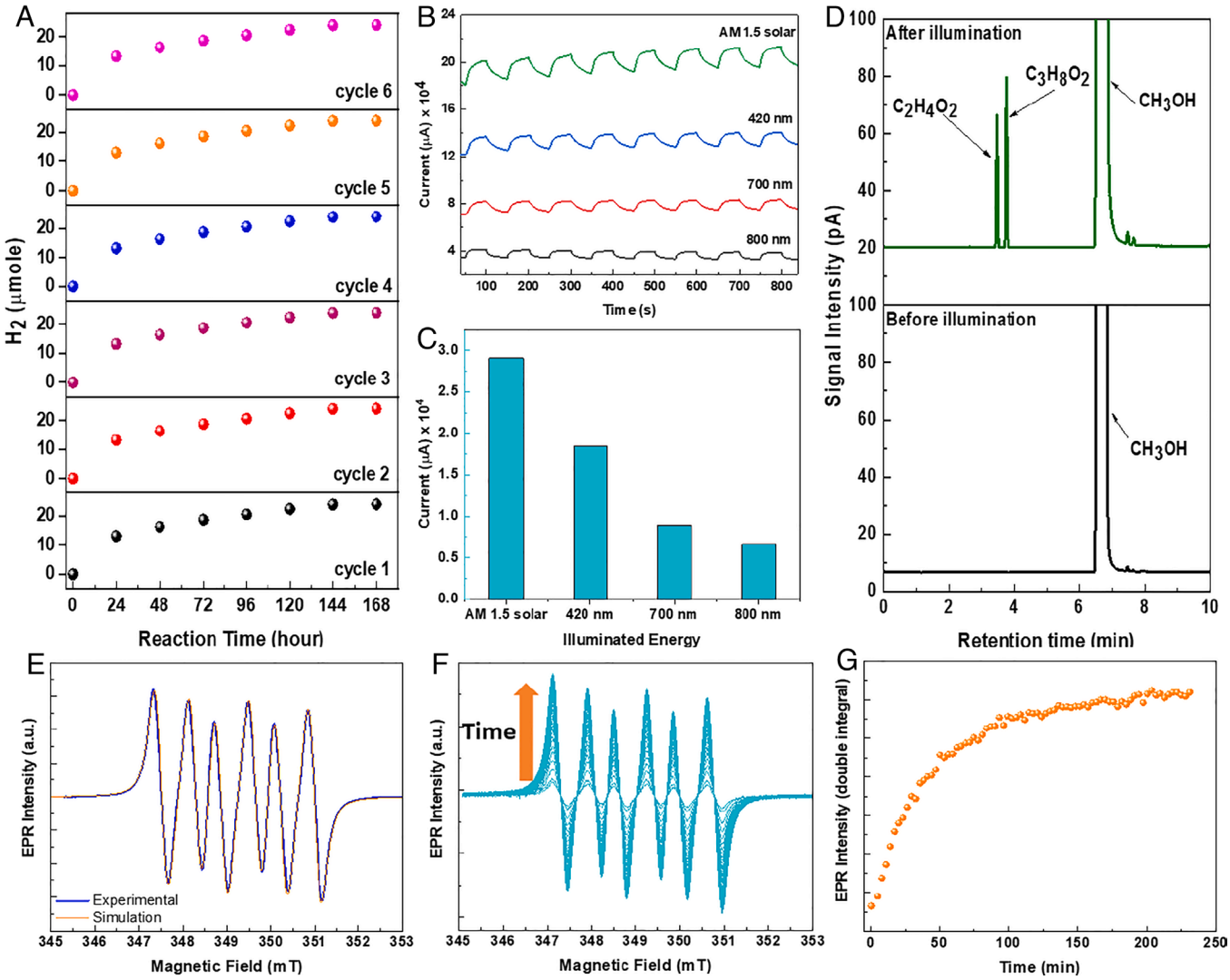

Fig. 4. Performance evaluation over plasmonic 2% Cu–WC/W catalysts. (*A*) H_2 evolution for six consecutive cycles. (*B*) Photocurrent at various wavelengths as a function of the time when light was on or off at 1.0 V against Ag/AgCl electrode in 0.1 M KOH aqueous solution containing pure CH_3OH. Note that the wavelength of 420, 700, and 800 nm corresponds to the centered wavelength of the employed band pass filters with 30 nm band width. (*C*) Photocurrent at various illuminated wavelengths. (*D*) Identified liquid products before and after illumination. (*E*) Electron paramagnetic resonance (EPR) profile of the methanol photodecomposition intermediate complexed to DMPO spin trap (see text). The resolved hyperfine coupling constants values of a_N = 1.36 mT and a_H = 0.78 mT are consistent with CH_3O* formation (15, 41). (*F*) EPR in situ illumination time series of the same sample where the arrow represents increasing illumination time. (*G*) Kinetic profile of the steady-state population of free radical trapped during illumination. Each data point in the kinetic profile represents each of the raw EPR spectra of (*F*).

it was 19.06% for $C_2H_4O_2$ (*SI Appendix*, Figs. S26–S29). As we did not observe any other carbon-related products irrespective of their formation type (gaseous or liquid), we conclude that the plasmon-induced CH_3OH decomposition into H_2 completely avoids CO_x products formation (*SI Appendix*, Fig. S30).

Methanol reforming into H_2 under solar light is expected to proceed selectively through a complex series of steps that require cleavage of methanol's O–H bond (14, 15) and typically involve a free radical intermediate. This radical intermediate is short lived but can be trapped by complexation with spin traps such as 5, 5-dimethyl-1-pyrroline N-oxide (DMPO). The resultant DMPO-radical adduct may be probed by EPR, whose spectral structure is diagnostic of the trapped radical (41). Fig. 4*E* shows the EPR spectrum of a 2% Cu–WC/W NP, DMPO, methanol suspension under continuous, in situ illumination and is consistent with the formation of the DMPO-OCH_3 adduct (41). This indicates CH_3OH decomposition proceeds through the CH_3O* (oxygen centered) free radical intermediate (41). A control experiment was also performed on a noncopper-bearing WC/W sample which did not display any significant free-radical component (*SI Appendix*, Fig. S31). Time-dependent in situ EPR showed only a small background DMPO-OCH_3 adduct signal prior to illumination (first EPR spectra in Fig. 4*F* when t = 0). Illumination with a white light source led to the accumulation of a DMPO-OCH_3 EPR signal (Fig. 4*F*) which subsequently decayed upon switching the light source off. The steady-state population of the DMPO-OCH_3 adduct signal increased during the entire illumination period (200 min), particularly during the first 50 min of illumination (Fig. 4*G*), demonstrating that the catalysts remain active. We note that in measurements where we excluded wavelengths shorter than 420 nm, we could not generate an appreciable/measurable steady state DMPO-OCH_3 adduct population, consistent with the fall off in photocurrents observed at longer wavelengths, suggesting that methanol photoreforming is more efficiently driven by blue light excitation, as expected.

Mechanistic Study. We performed FDTD and density functional theory (DFT) simulations to study LSPR's local E-field distribution

and to probe the effects of microenvironments (strain field and/or E-field) on the underlying CH_3OH photoreforming reactions at the Cu–WC/W NPs. To discover plasmonic behavior from FDTD simulation, we considered different wavelengths and directions of the incident light relative to the Cu NPs mounted on WC/W (Fig. 5 *A*–*E* and *SI Appendix*, Fig. S32). It is widely believed that upon light illumination, the incident photons interact with the conduction electrons of the plasmonic metal NPs resulting in the excitation of LSPR. The LSPR acts to confine the photon energy and generate strong local E-fields via enhanced light absorption at the surfaces of metallic NPs (42). The energy of these elevated fields can be dissipated through either radiative reemission of photons or nonradiative excitation of energetic charge carriers (hot e^-/h^+) which could transfer to nearby materials. On the other hand, these elevated fields, kinds of reaction microenvironments, could perturb/tailor the surrounding catalytic activities of catalysts. As observed, the local surface E-field intensity was enhanced (doubled) for WC/W (Fig. 5*B*), which is supposed to be dominated by SWIR LSPR of WC/W afore-discussed. Especially, the tops near the Cu NPs are covered by the extended E-field of the Cu LSPR (Fig. 5 *C*–*E*), indicating that the Cu NPs introduce more light absorption and then provide more carriers for the CH_3OH reforming on WC. In addition, broadband visible-to-NIR light absorption from Cu NPs and SWIR absorption from WC/W jointly satisfy the sufficient utilization of light in different energy ranges (Fig. 3 *C*–*E*). However, the freestanding Cu and WC samples underperformed in CH_3OH reforming because of their relatively high reaction energy barriers (*SI Appendix*, Fig. S33).

To understand the strain effects on CH_3OH photoreforming reactions, we performed DFT calculations to compute the free energy of reaction pathways. The compressive strain on WC from W due to a lattice mismatch has an appreciable impact on reducing reaction barriers (Fig. 5*F*). Without any external field perturbation (black pathways), the first reforming/dehydrogenation step ($CH_3OH^* \rightarrow CH_3O^*$) occurs easily on WC, which is exothermic in nature. Next, the dehydrogenation of CH_3O^* faces the energy barrier of 0.73 eV, which is the rate-determining step ($CH_3O^* \rightarrow HCHO^*$) under no external field perturbation. However, when the strain field is applied on WC, the rate-determining step shifts to $CHO^* \rightarrow CO^*$ (orange pathways) from $CH_3O^* \rightarrow HCHO^*$. The PC rate-determining step shift is caused by different lattice spacings and has been reported elsewhere (43, 44). With lattice misfits, the WC NPs show a reaction barrier at 0.38 eV, much lower than the 0.73 eV barrier of WC (black pathways). In addition, we employ cluster models to evaluate 5 states (1 ground state and 4 exited states) to evaluate the CH_3OH dehydrogenation reactions. Compared with the ground state, the excited state provides slight corrections to the energy. The same conclusion can be drawn from the ground-state periodic DFT when considering strain: Strain lowers the reaction activation barrier in the ground state, and the barrier is further lowered upon considering electronic excitation (*SI Appendix*, Tables S6 and S7 and Figs. S34 and S35). This conclusion is consistent with the qualitative analysis between the relative energy paths predicted by DFT and higher-level (second-order multireference perturbation theory) simulations for light-driven methane dry reforming on the CuRu surface (45).

As noticed, when the E-field was applied to Cu, its effect on the energy barrier of the rate-determining step during methanol photoreforming is insignificant (*SI Appendix*, Fig. S36). However, when WC is under the E-field condition, the rate-determining step ($CH_3O^* \rightarrow HCHO^*$) has an energy barrier of 0.55 eV (Fig. 5*F*, red pathways), which is lower than 0.73 eV relative to WC under no perturbation. Impressively, when E-field and strain field are combined, the effect on the WC catalysis is greatly enhanced with the reaction barrier being significantly reduced (green pathways). The reaction barrier for the $CHO^* \rightarrow CO^*$ step is 0.3 eV which is sufficient to block the further oxidation of CO^* species to form any CO and/or CO_2 in the reaction which is consistent with experimental observation. However, the formed CO^* species could combine with the available intermediates to form methyl formate ($HCOOCH_3$), followed up in *SI Appendix*, Supporting text. Note that Cu NPs induced extra enhancement of the local field, i.e., two times enhanced compared with the E-field at WC surface. A combined effect of Cu LSPR-induced local field enhancement and strain field was also studied, highlighting that the effect from ×4 E-field does not change much from that under ×2 E-field (*SI Appendix*, Fig. S37). Mechanistic studies reveal that the dynamics of methanol photoreforming are mainly attributed to the combined microenvironments (strain and E-field) perturbation in WC and energetic charge carriers supplied from Cu LSPR due to its broadband solar absorption. The heterojunction formed by plasmonic Cu NPs and the WC/W NPs will promote the enhancement of the local electric field of Cu (*SI Appendix*, Fig. S38), thereby generating stronger surface plasmons with providing more hot charge carriers toward the nearby active sites of WC surfaces for catalysis enhancement. This makes the oxidation of CH_3O^* into $HCHO^*$ easier, while the adsorption of CH_3O^* on the WC surface through a single field is not enough to significantly reduce the reaction energy barrier. Moreover, the changes of the rate-determining steps due to strain field would prolong the photoreforming and thus more H^+ to form H_2, significantly improving the production of H_2 while simultaneously suppressing the formation of CO and/or CO_2. DFT calculations show that the efficient CH_3OH photoreforming to zero-emission H_2 fuel is associated with the desirable tailoring of reaction pathways under strain and E-field coperturbation with a synergistic charge carrier supply from the Cu of Cu–WC/W NPs hybrid system, which has been schematically represented in Fig. 5*G*. A general discussion on methanol reforming to H_2 along with other products formation under plasmonic excitation is included in the *SI Appendix*, Supporting text.

Discussion

Here, we demonstrated the first example of a nontraditional plasmonic nanohybrid structure between Cu and WC/W NPs using a carburization process. We found a 2% loading of Cu–WC/W NPs led to efficient liquid CH_3OH photoreforming under ambient conditions. The photocatalyst is highly durable and free from CO_x formation. Computational studies uncover that the perturbation of local microenvironments regulates the reaction kinetics of methanol dehydrogenation on WC surfaces, reducing the oxidation barrier of methanol while maintaining an uphill barrier in the last reaction step to avoid CO_x formation. The energetic charge carriers from Cu's broadband solar absorption favorably flow to WC surfaces driven by their optical dielectric constants difference. The microenvironments (strain and E-field) coperturbation and charged carriers provision enabled the efficient and stable CH_3OH photoreforming to form autoseparable pure H_2 fuel and C_3 (i.e., $C_3H_8O_2$)-dominated liquid products. It is hoped that this work will provide guiding principles in synergizing microenvironments with plasmonic photocatalysis for sustainable solar fuel production based on abundant and inexpensive elements under the ambient conditions.

Materials and Methods

Chemicals. Urea (ACS reagent, 99%), copper (II) chloride ($CuCl_2$, 97%), tungstic acid (H_2WO_4, 99%), alcohols such as methanol (HPLC grade, 99.9%), ethanol

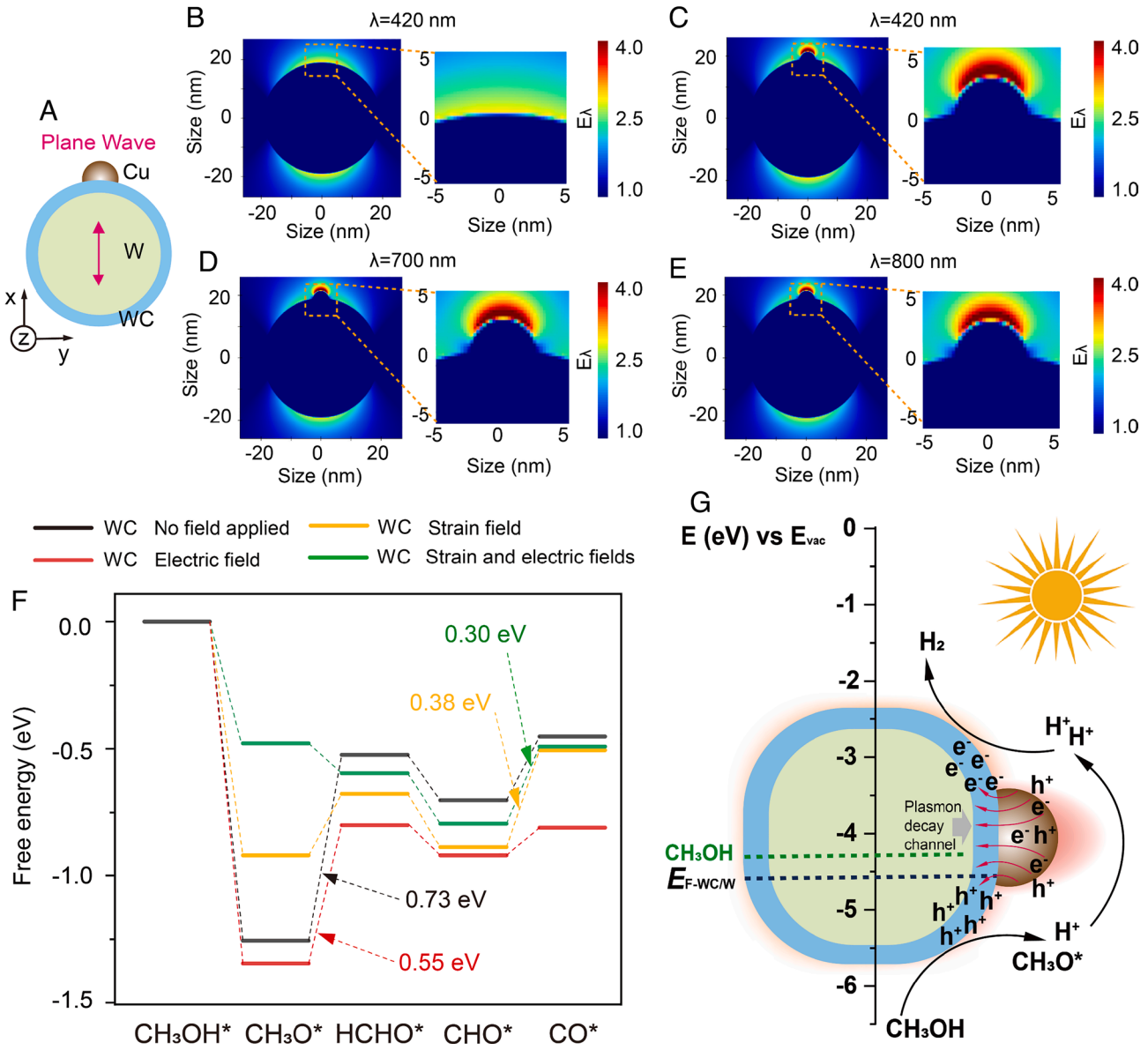

Fig. 5. FDTD and DFT simulation study. (*A*) Schematic representation of the Cu NP embedded on a WC/W substrate. (*B–E*) Schematics (*Left*) and partial zoom (*Right*) showing the enhancement of E-field intensity induced by WC/W. (*C–E*) Wavelength effects on the distributions of the E-field strength for the Cu NP embedded on a WC/W substrate. The enhancement of E-field intensity induced by introducing Cu NPs is compared by (*B*) and (*C–E*). (*F*) Free-energy diagram for methanol photoreforming calculated by DFT, where the perturbations from the strain field (compressive strain for {110} and {001} planes of WC are 12% and 21%, respectively), E-field (867.93 V/m under ×2 enhancement), or both were applied. (*G*) Photocatalytic mechanism insights of dual-fields tuned WC activity in Cu–WC/W junctions for selective methanol to H_2 and multicarbon products. The elevated local E-field surrounding the Cu NP surface are schematically presented. The Fermi level E_F, i.e., work function (WF), of WC/W and 2% Cu–WC/W is estimated to be 4.57 and 4.34 eV, respectively, relative to vacuum from the extrapolation of corresponding UPS kinetics profiles (Fig. 2*F*). As the reported WF of metallic Cu is 4.1 to 4.5 eV (46) lower than that of WC/W, it is reasonable to say the WF of 2% Cu–WC/W was reduced slightly after loading Cu onto WC/W. The methanol oxidation potential is ~−4.3 eV (9) as indicated by the green dotted line; and the E_F of WC/W is −4.57 eV, as indicated by the black dotted line which is more negative to CH_3OH potential (~−4.3 eV). This favors the energetic charge carriers/holes to oxidize methanol molecules near the surface of WC, with releasing protons for H_2 production. The energetic charge carriers (hot e^--h^+ pairs) could flow from Cu to WC by dissipating the energy via plasmon decay channel because of the higher imaginary part of dielectric function of WC than Cu NPs. In addition, as WC and Cu NPs are in close proximity, the direct, higher, energy absorption of WC shell from localized field intensities of Cu LSPR at the junction could also push up more e^--h^+ formation there.

(HPLC grade, 99.5%), methylal ($C_3H_8O_2$, 99%), methyl formate ($C_2H_4O_2$, 99%), and free radical spin trapping reagent 5, and 5-dimethyl-1-pyrroline N-oxide (DMPO, 97%) were all purchased from Sigma Aldrich. Pure H_2 (99.999%), and Ar (99.997%) were purchased from BOC gas, Australia.

Catalysts Preparation. A simple procedure was followed to synthesize the Cu–WC/W plasmonic NPs with varying loading conditions. Initially, we mixed urea and tungstic acid precursor in 2 mL ethanol solution, keeping total weight not exceeding 2.0 g. Later, we added the desired amount of noble-free Cu precursor into the above mixture. After this, we stirred the mixture for a couple of hours and aged the mixture for whole nights following 3 h of annealing in 850 °C under H_2 vacuum atmosphere. Once the annealing process was done, we did the passivation of the materials until the CVD temperature reached room temperature. The prepared materials were used without any further treatment. Unless otherwise stated, a very identical synthetic approach was used to prepare other samples in this work.

Catalysts Characterization. Aberration-corrected (Cs corrector) high-resolution TEM experiments were performed on an FEI Titan 80 to 300 microscope at 300 kV, which was equipped with a 2k × 2k Gatan UltraScan 1000 CCD camera. HAADF STEM imaging and EDX mapping analysis were conducted using a Hitachi HF5000 at 200 kv, which is a cold FEG TEM/STEM with a Cs probe corrector equipped

with double EDX Ultra 100 detector from Oxford Instruments. The misfit of the coherent interface between W and WC were calculated by using the formula of {d(WC)-d(W)}/d(WC). Scanning electron microscopy (SEM) samples were prepared by sonicating powder/ethanol mixture and then drying the suspensions onto a silica substrate. Sample analysis was performed by using a field-emission SEM (ZEISS Sigma 300) operated at 5.0 kV. Ultraviolet-Diffuse reflectance spectrophotometer (UV-DRS) measurement was conducted on a Lamda 465 (Serial No: 465K7121104, PerkinElmer) instrument. A blank without a sample was measured as background before testing the samples. Powder XRD measurement was done on a PANalytical Empyrean using Cu Kα (λ = 1.5406 Å) radiation with a generator voltage and current of 45 kV and 40 mA, respectively. XPS and ultraviolet photoemission spectroscopy (UPS) were performed on a Nexsa (ThermoFisher Scientific) spectrometer and the Surface, Interface, and Nanostructure Science (SINS) beamline at the Singapore Synchrotron Light Source (SSLS). The system work function was calibrated for each sample by setting the main line of the C 1s spectrum to 284.8 eV. At the SINS beamline, high-resolution XPS data were recorded under ultrahigh vacuum conditions with a base pressure of 1×10^{-10} mbar. For the characterization of the respective core-level spectra, the photon energy was calibrated using the Au $4f_{7/2}$ core-level peak at 84.0 eV of a gold foil that was sputter-cleaned in electrical contact with the sample. All spectra were collected at the normal emission using a VG Scienta R4000 analyzer, and the data were normalized by the photon current. Meanwhile, the work function was determined by employing −10 V applied bias to the sample. Each high-resolution spectrum was fitted with a Gaussian-Lorentzian (70 to 30%) line shape using a Shirley background.

Electron paramagnetic resonance (EPR) measurement was done on a commercial Bruker E550 spectrometer equipped with an ER 4130TM resonator with the following parameters: 150 mW, 9.8 GHz light, and 1 G modulation amplitude. Liquid solution EPR measurements were analyzed using a quartz flat cell. For spin trap experiments, PC samples were dispersed in 10 mL methanol, followed by solar illumination for 2 h at room temperature. A small volume of the illuminated solution was then mixed with a DMPO aqueous solution (150 mM). The reaction mixture was then used for EPR measurement. For reference purpose, an aliquot of this mixture was taken prior to illumination and its EPR spectrum was recorded. Time-dependent in-situ EPR measurements were done in an analogous manner except DMPO was added to the sample prior to illumination which was performed inside the resonant cavity of the spectrometer during sample acquisition. In situ illumination was achieved by a 250 W quartz-halogen lamp whose beam was passed through a water filter and lens and was focused on the sample. X-ray absorption near-edge structure (XANES) experiments were done at the National Synchrotron Radiation Research Center, Hsinchu, Taiwan. Cu K-edge spectra were acquired at Wiggler beamline 17C and 07A using a Lytle cell or transmission cell. A double-crystal Si (111) monochromator was used with an energy resolution $\Delta E/E$ better than 2×10^{-4}. At Cu-K edge, and the energy resolutions were about in the range of 8,770 to 9,840 eV. The focused beam size at the sample position was 4 mm × 2 mm. Athena software (47) was utilized to process and analyze the raw XAS data including background removal, edge-step normalization, and Fourier transform. Artemis software (47) was used to fit the Fourier-transformed EXAFS data with a model. The normalized $\chi(E)$ was transformed from energy space to k-space using Artemis software. The k^2-weighted $\chi(k)$ data in the k-space ranging from 3.0 to 10.5 $Å^{-1}$ at Cu K-edge was Fourier transformed (FT) to r-space to isolate the EXAFS contributions from different coordination shells. The fitting of EXAFS data was done for only Cu–Cu first shell in r-space ranging from 1 to 3.0 Å by using a nonlinear least squares algorithm. Phases and amplitudes have been calculated by FEFF8 code using the Artemis software (47). A conventional three-electrode system was used to measure electrochemical impedance, in which saturated Ag/AgCl electrode, Pt wire, and glassy carbon electrode (diameter ~ 3 mm) with photocatalysts (loading density ~ 0.28 mg cm^{-2}) act as reference, counter, and working electrodes, respectively. The electrical signal from the above electrode system was processed by PARSTAT 3000 station with 1.2 kHz frequency at a constant voltage of 1.0 V against Ag/AgCl scale. Photocurrent measurement was performed using the same instrumentations above in which the solar light switching on and off condition was controlled manually keeping the elapsed time interval identical. Wavelength-dependent photocurrent measurement was done by varying the filter to 420, 700, and 800 nm, whereas control experiment was done at AM 1.5 G solar illuminated conditions. All these experiments were performed in pure CH_3OH solution using 0.1 M KOH electrolyte at 1.0 volts in the scale of Ag/AgCl. Nuclear magnetic resonance spectroscopy was done on a Bruker 400 MHz instrument keeping the ratio of sample to deuterated methanol (CD_3OD) at 4:3 to identify the ^1H species before and after reaction. Inductively coupled plasma (ICP) was performed using the Agilent ICPOES720 (America Agilent). Samples were digested in 6 mL nitric acid, 2 mL hydrofluoric acid, 1 mL hydrogen peroxide, and 2 mL hydrochloric acid and then heated for 10 h. After cooling, the digested samples were transferred into flasks and brought to the final volume with Milli-Q water and then analyzed by ICP-OES.

PC Experiment. PC methanol decomposition reactions were performed in a 15 mL quartz bottle under ambient working conditions. Atop of the bottle, a silicone rubber septum (diameter ~ 13 mm, thickness ~3 mm, Specialty Silicone Products, Inc.) was fixed to contain the gaseous products from reactions. A 300 W Xenon lamp source (Microsolar300, Beijing Perfectlight Technology Co., Ltd) with an AM 1.5 G filter was horizontally placed to concentrate the light on the reaction solution. Band pass filters with center positions at 420, 700, and 800 nm were used to do other experiments where needed. Depending on the type of experiments, a desired amount of photocatalyst was added into the reactor while 90 min sonication was performed to disperse the photocatalysts in 10 mL CH_3OH solution. To remove any residual air contamination from the reactor bottle, the degassing was done using Ar at least for a half hour. Gas chromatography, GC, (Nexis 2030, Shimadzu Scientific instruments) was utilized to detect gaseous products from the reaction which was housed with a thermal conductivity detector, a flame ionization detector (FID), and a ShinCarbon (100/120, 1 mm ID, 1/16″ OD) column. Using a 100-μL Hamilton syringe (Hamilton company Inc.), 50 μL of gaseous species from the empty space of the reactor bottle was injected in GC before being illuminated by the light which works as a reference point. Next, we followed the similar approach to inject the formed gaseous products after illumination and record the peak area (PA) from GC. A standard calibration curve of pure hydrogen was utilized to quantify the formed gaseous products. The duration of each PC test relied on the type of experiments, for example, the stability test was continued for several days, whereas the catalyst screening test lasted typically for 120 min. Liquid products identification after illumination was done on Agilent 7890 A GC housed with an FID and 7010 Triple Quadruple GC/MS/MS with helium as the carrier gas. Injections were split in 100:1 with a split flow of 150 mL/min and delivered through an autosampler. The inlet temperature was 220 °C, while oven temperature was set in the range of 40 to 240 °C, among which a ramping rate of 5 °C/min was applied in the range of 40 to 100 °C with no hold time and another ramping rate of 20 °C/min used in the range of 100 to 240 °C with a hole time of 3.5 min. Scans were measured from 10 mass to 300 mass using 300 ms scan time. The FID temperature was set to 250 °C, and the injection volume was 1 μL. National Institute of Standards and Technology (NIST), USA, MS spectral Library was utilized to match and authenticate the formed liquid products after the reaction.

Hot Filtration Test. The photoirradiation of methanol to hydrogen production for 12 h followed the similar PC experimental procedure as described in the main text. After 12 h of light illumination, we stopped the reaction and took out the catalytic materials using the filter paper (Merck Millipore Mixed Cellulose Ester Membrane Filters, porosity 0.22 μm, diameter 13 mm, Australian Scientific Pty Ltd). Next, we heat the filtered methanol solution for other three-time 12 h while doing the H_2 production analysis at 25, 35, and 50 °C, respectively. To provide a uniform heat distribution surrounding the filtered methanol solution, we submerged the reaction quartz bottle inside the oil bath and stirred the filtered methanol solution using a magnetic bar. During 12 h of heating, we did the GC measurement for H_2 generation after 2, 6, and 12 h, respectively.

Thermal Test. The experimental procedure for the thermal effect is similar to PC experimental conditions but without the light illumination. We kept the catalyst-dispersed methanol solution at 25, 35, 50, and 65 °C for 6 h and did the H_2 production analysis using the GC instrument under dark settings at the beginning, followed by two more measurements at 2 and 6 h, respectively. To provide a homogenous temperature gradient around the reaction bottle, we submerged the reaction quartz bottle inside the oil bath and stirred the methanol solution using a magnetic bar with 350 rpm.

LSPR Measurement. STEM-Electron energy loss spectroscopy (EELS) was performed in the FEI Titan G3 50-300 PICO at 80 kV equipped with a Schottky type high-brightness electron gun (FEI X-FEG), a monochromator unit, a Cs probe

corrector (CEOS DCOR), a Cs-Cc achro-aplanat image corrector (CEOS CCOR+), a post-column energy filter system (Gatan Quantum 966 ERS), and a 16 megapixel CCD system (Gatan UltraScan 4000 UHS). The energy resolution of 130 meV was obtained. An EELS spectrum was acquired from an individual copper particle on WC/W NP. To excite its plasmon resonance, the electron probe was parked 2 to 3 nm next to the copper particle (48). For comparison, a spectrum was acquired from WC/W NP in the same way.

Theoretical Calculation. The theoretical finite difference time domain (FDTD) simulations were performed by using Lumerical (FDTD solutions, Lumerical Solutions, Inc.) software. The Cu/W/WC system was modeled as a 38-nm diameter sphere, where the diameter of WC was 30 nm, the thickness of WC was 4 nm, and the diameter of Cu particles attached to the WC surface was 5 nm. All the optical parameters used in FDTD simulation were calculated from the results of DFT calculations. We assumed that the background medium was the air with an index of refraction of 1.0. A total field-scattered field source of light consisting of plane waves was used as the incident light source. A uniform grid size of 0.25 nm (x, y, and z) was accepted to ensure the accuracy of E-field calculations. A frequency domain field distribution monitor was used to evaluate the E-field distribution of the Cu/W/WC system. The perfectly matched layer absorbing boundary conditions was considered. The E-field magnitude from the incident light was received by following steps (49):

$$I_{ave} = c\in_0 E_0^2 / 2,$$

$$E_0 = (2I_{ave}/c\in 0)^{1/2},$$

where I_{ave} is the intensity of incident solar simulator (100 mW/cm^2), c is the speed of light, ε_0 is the permittivity of free space, and E_0 is the maximum E-field strength. The calculated E-field magnitude is 868 V/m.

All DFT calculations were performed by using the Vienna ab initio Simulation Package (VASP) code (50). Projector Augmented Wave pseudopotentials were used to process the core electrons, and the Perdew–Burke–Ernzerhof function of the generalized gradient approximation was used to describe electron exchange and related interactions. The cutoff energy of the plane wave basis set was 400 eV, and the convergence criteria for energy and force are less than 10^{-4} eV and 10^{-2} eV/Å, respectively. In addition, the van der Waals correction was corrected for the dispersion correction using Grimme's DFT-D3 method as implemented in VASP. For calculating optical properties, the Heyd–Scuseria–Elnzehof (HSE06) screened hybrid functional was adopted and the Brillouin zone was sampled with 30 × 30 × 30 Monkhorst-Pack grids. The constructed slab model for calculating free energy was guaranteed to be larger than 10 Å in the a, b direction to avoid the interactions caused by periodicity. The c direction was set to ensure that the vacuum distance was not less than 15 Å to avoid interlayer interactions. The Brillouin zone was sampled with 3 × 3 × 1 Monkhorst-Pack grids for calculating free energy. Detailed tests for the convergence of layer number for surface energy for Cu and W are shown in *SI Appendix*, Tables S2 and S3. Calculated the surface energy and Work function for Cu surface with low Miller index for Cu and W were used to determine the most stable exposed crystal facets in *SI Appendix*, Tables S4 and S5.

Data, Materials, and Software Availability. All study data are included in the article and/or *SI Appendix*.

ACKNOWLEDGMENTS. We gratefully acknowledge the support from the Australian National University (ANU) Futures Scheme (Q4601024) and National Natural Science Foundation of China (52173234). The authors thank Dr. Juri Barthel and Dr. Janghyun Jo (Forschungszentrum Jülich GmbH) for the help on alignment of PICO and monochromator. JDE is supported by a Ramsay Fellowship from the University of Adelaide. ZIH Dresden and Phoenix HPC service at the University of Adelaide are thanked for providing high-performance computing resources. This project was undertaken with the assistance of resources and services from the National Computational Infrastructure (NCI), which is supported by the Australian Government.

Author affiliations: [a]Research School of Chemistry, Australian National University, Canberra ACT 2601, Australia; [b]Materials Interfaces Center, Shenzhen Institute of Advanced Technology, Chinese Academy of Sciences, Shenzhen, Guangdong 518055, P.R. China; [c]Ernst Ruska-Centre for Microscopy and Spectroscopy with Electrons, Forschungzentrum Jülich GmbH 52428, Jülich, Germany; [d]Research School of Electrical, Energy and Materials Engineering, Australian National University, Canberra ACT 2601, Australia; [e]Physics Department, Shanghai Key Laboratory of High Temperature Superconductors, Shanghai University, Shanghai 200444, P.R. China; [f]Department of Physics, Faculty of Science, National University of Singapore, Singapore 117542, Singapore; [g]Singapore Synchrotron Light Source, National University of Singapore, Singapore 117603, Singapore; [h]Centre for Advanced Nanomaterials and Department of Chemistry, Adelaide, The University of Adelaide, Adelaide SA 5000, Australia; [i]State Key Laboratory of Multiphase Flow in Power Engineering, Xi'an Jiaotong University, Xi'an, Shaanxi 710049, P.R. China; and [j]Key Laboratory of Ocean Energy Utilization and Energy Conservation of Ministry of Education, School of Energy and Power Engineering, Dalian University of Technology, Dalian 116024, P.R. China

Author contributions: N.U. and X.Y. designed research; N.U., Z.S., J.L., H.L., P.C., A.W., C.S.T., H.T.N., J.D.E., X.L., X.Z., M.H., R.E.D.-B., H.Z., N.C., and Z.Y. performed research; J.D.E. contributed new reagents/analytic tools; N.U., Z.S., J.L., P.C., A.W., X.Y., H.T.N., J.D.E., X.Z., M.H., R.E.D.-B., A.T.S.W., H.Z., N.C., and Z.Y. analyzed data; and N.U., Z.S., J.L., P.C., X.Y., X.Z., M.H., R.E.D.-B., A.T.S.W., H.Z., N.C., and Z.Y. wrote the paper.

1. J. Liu *et al.*, Metal-free efficient photocatalyst for stable visible water splitting via a two-electron pathway. *Science* **347**, 970–974 (2015).
2. X. Liu *et al.*, Enhanced localized dipole of Pt-Au single-site catalyst for solar water splitting. *Proc. Natl. Acad. Sci. U.S.A.* **119**, e2119723119 (2022).
3. Y. Inoue, K. Sato, K. Sato, H. Miyama, A device type photocatalyst using oppositely polarized ferroelectric substrates. *Chem. Phys. Lett.* **129**, 79–81 (1986).
4. J. B. Joo *et al.*, Promotion of atomic hydrogen recombination as an alternative to electron trapping for the role of metals in the photocatalytic production of H_2. *Proc. Natl. Acad. Sci. U.S.A.* **111**, 7942–7947 (2014).
5. D. Zhao *et al.*, Boron-doped nitrogen-deficient carbon nitride-based Z-scheme heterostructures for photocatalytic overall water splitting. *Nat. Energy* **6**, 388–397 (2021).
6. M. Liu *et al.*, Photocatalytic hydrogen production using twinned nanocrystals and an unanchored NiS_x co-catalyst. *Nat. Energy* **1**, 16151 (2016).
7. L. Zhou *et al.*, Quantifying hot carrier and thermal contributions in plasmonic photocatalysis. *Science* **362**, 69–72 (2018).
8. Y. Liu *et al.*, In situ construction of fibrous AgNPs/g-C_3N_4 aerogel toward light-driven COx-free methanol dehydrogenation at room temperature. *Chem. Eng. J.* **334**, 2401–2407 (2018).
9. Z. Liu *et al.*, Room temperature stable COx-free H_2 production from methanol with magnesium oxide nanophotocatalysts. *Sci. Adv.* **2**, e1501425 (2016).
10. G. Halasi, G. Schubert, F. Solymosi, Comparative study on the photocatalytic decomposition of methanol on TiO_2 modified by N and promoted by metals. *J. Catal.* **294**, 199–206 (2012).
11. M. Murdoch *et al.*, The effect of gold loading and particle size on photocatalytic hydrogen production from ethanol over Au/TiO_2 nanoparticles. *Nat. Chem.* **3**, 489–492 (2011).
12. X. Bai *et al.*, Ambient sunlight-driven photothermal methanol dehydrogenation for syngas production with 32.9% solar-to-hydrogen conversion efficiency. *iScience* **24**, 102056 (2021).
13. A. Gazsi, G. Schubert, T. Bánsági, F. Solymosi, Photocatalytic decompositions of methanol and ethanol on Au supported by pure or N-doped TiO_2. *J. Photochem. Photobiol. A Chem.* **271**, 45–55 (2013).
14. Y. Pang *et al.*, Colloidal single-layer photocatalysts for methanol-storable solar H_2 fuel. *Adv. Mater.* **31**, 1905540 (2019).
15. N. Uddin *et al.*, Zero-emission multivalorization of light alcohols with self-separable pure H_2 fuel. *Appl. Catal. B Environ.* **292**, 120212 (2021).
16. H. Lu *et al.*, Noble-metal-free multicomponent nanointegration for sustainable energy conversion. *Chem. Rev.* **121**, 10271–10366 (2021).
17. S. Yu, S. Louisia, P. Yang, The interactive dynamics of nanocatalyst structure and microenvironment during electrochemical CO_2 conversion. *JACS Au* **2**, 562–572 (2022).
18. L. Dong, W. Chen, C. Zheng, N. Deng, Microstructure and properties characterization of tungsten–copper composite materials doped with graphene. *J. Alloy Comp.* **695**, 1637–1646 (2017).
19. M. Katoh, H. Kawarada, Heteroepitaxial growth of tungsten carbide films on W (110) by plasma-enhanced chemical vapor deposition. *Jpn J. Appl. Phys.* **34**, 3628 (1995).
20. S. E. Habas, H. Lee, V. Radmilovic, G. A. Somorjai, P. Yang, Shaping binary metal nanocrystals through epitaxial seeded growth. *Nat. Mater.* **6**, 692–697 (2007).
21. J. Zhang, Y. Tang, K. Lee, M. Ouyang, Nonepitaxial growth of hybrid core-shell nanostructures with large lattice mismatches. *Science* **327**, 1634–1638 (2010).
22. Z. Chen *et al.*, Eutectoid-structured WC/W_2C heterostructures: A new platform for long-term alkaline hydrogen evolution reaction at low overpotentials. *Nano Energy* **68**, 104335 (2020).
23. M. Shao *et al.*, WXy/g-C_3N_4 (WXy=W_2C, WS_2, or W_2N) Composites for highly efficient photocatalytic water splitting. *ChemSusChem* **12**, 3355–3362 (2019).
24. X. Xu *et al.*, Enriching hot electrons via nir-photon-excited plasmon in WS_2@Cu hybrids for full-spectrum solar hydrogen evolution. *Adv. Funct. Mater.* **28**, 1804055 (2018).
25. P. Kirsch, J. Ekerdt, Chemical and thermal reduction of thin films of copper (II) oxide and copper (I) oxide. *J. Appl. Phys.* **90**, 4256–4264 (2001).
26. M. C. Biesinger, Advanced analysis of copper X-ray photoelectron spectra. *Surf. Interface Anal.* **49**, 1325–1334 (2017).
27. E. Borfecchia *et al.*, Evolution of active sites during selective oxidation of methane to methanol over Cu-CHA and Cu-MOR zeolites as monitored by operando XAS. *Catal. Today* **333**, 17–27 (2019).
28. G. V. Korshin, A. I. Frenkel, E. A. Stern, EXAFS study of the inner shell structure in Copper(II) complexes with humic substances. *Environ. Sci. Technol.* **32**, 2699–2705 (1998).
29. X. L. Du, Z. Jiang, D. S. Su, J. Q. Wang, Research progress on the indirect hydrogenation of carbon dioxide to methanol. *ChemSusChem* **9**, 322–332 (2016).
30. S.-C. Yang *et al.*, Synergy between Ceria oxygen vacancies and Cu nanoparticles facilitates the catalytic conversion of CO_2 to CO under mild conditions. *ACS Catal.* **8**, 12056–12066 (2018).
31. U. Aslam, V. G. Rao, S. Chavez, S. Linic, Catalytic conversion of solar to chemical energy on plasmonic metal nanostructures. *Nat. Catal.* **1**, 656–665 (2018).

32. C. Ren *et al.*, ZnSe nanoparticles with bulk WC as cocatalyst: A novel and noble-metal-free heterojunction photocatalyst for enhancing photocatalytic hydrogen evolution under visible light irradiation. *Appl. Mater. Today* **20**, 100731 (2020).
33. Y. Lin *et al.*, Copper nanoparticles with near-unity, omnidirectional, and broadband optical absorption for highly efficient solar steam generation. *Nanotechnol.* **30**, 015402 (2018).
34. L. Ren *et al.*, Designing carbonized loofah sponge architectures with plasmonic Cu nanoparticles encapsulated in graphitic layers for highly efficient solar vapor generation. *Nano Lett.* **21**, 1709–1715 (2021).
35. X. Chen, D. Wu, P. Zhou, M. Chen, H. Yan, Modeling the solar absorption performance of copper@ carbon core–shell nanoparticles. *J. Mater. Sci.* **56**, 13659–13672 (2021).
36. X. Chen, P. Zhou, H. Yan, M. Chen, Systematically investigating solar absorption performance of plasmonic nanoparticles. *Energy* **216**, 119254 (2021).
37. Y. Xu *et al.*, Cu@C core-shell nanoparticles with efficient optical absorption: DDA-based simulation and experimental validation. *Res. Phys.* **16**, 102885 (2020).
38. S. L. Wang *et al.*, 2D WC/WO_3 heterogeneous hybrid for photocatalytic decomposition of organic compounds with Vis–NIR light. *Adv. Funct. Mater.* **28**, 1705357 (2018).
39. B. Wei, S. Jian, A near-infrared perfect absorber assisted by tungsten-covered ridges. *Plasmonics* **14**, 179–185 (2019).
40. M. L. Brongersma, N. J. Halas, P. Nordlander, Plasmon-induced hot carrier science and technology. *Nat. Nanotechnol.* **10**, 25–34 (2015).
41. S. Xie *et al.*, Visible light-driven C—H activation and C-C coupling of methanol into ethylene glycol. *Nat. Commun.* **9**, 1181 (2018).
42. S. Chavez, U. Aslam, S. Linic, Design principles for directing energy and energetic charge flow in multicomponent plasmonic nanostructures. *ACS Energy Lett.* **3**, 1590–1596 (2018).
43. Y. Zhang, N. Zhou, K. Zhang, F. Yan, Plasmonic copper nanowire@ TiO_2 nanostructures for improving the performance of dye-sensitized solar cells. *J. Power Source* **342**, 292–300 (2017).
44. P. Yan *et al.*, The regulation of reaction processes and rate-limiting steps for efficient photocatalytic CO_2 reduction into methane over the tailored facets of TiO_2. *Catal. Sci. Technol.* **9**, 1451–1456 (2019).
45. P. Li *et al.*, Crystal facet-dependent CO_2 photoreduction over porous ZnO nanocatalysts. *ACS Appl. Mater. Interfaces* **12**, 56039–56048 (2020).
46. L. Zhou *et al.*, Light-driven methane dry reforming with single atomic site antenna-reactor plasmonic photocatalysts. *Nat. Energy* **5**, 61–70 (2020).
47. B. Ravel, M. Newville, ATHENA, ARTEMIS, HEPHAESTUS: Data analysis for X-ray absorption spectroscopy using IFEFFIT. *J. Synchrotron Radiat.* **12**, 537–541 (2005).
48. Z. Liu *et al.*, Photoactivity and stability co-enhancement: When localized plasmons meet oxygen vacancies in MgO. *Small* **14**, 1803233 (2018).
49. E. Hecht, *Optics 2nd Edition Addison* (Wesley Publishing Company, 1987).
50. G. Kresse, J. Furthmüller, Efficient iterative schemes for ab initio total-energy calculations using a plane-wave basis set. *Phys. Rev. B* **54**, 11169 (1996).